


# Light-cone-like spreading of single-particle correlations in the Bose-Hubbard model after a quantum quench in the strong-coupling regime

Matthew R. C. Fitzpatrick\* and Malcolm P. Kennett†

*Department of Physics, Simon Fraser University, 8888 University Drive, Burnaby, British Columbia, Canada, V5A 1S6*

 (Received 18 July 2018; published 19 November 2018; corrected 4 March 2019)

We study the spreading of correlations in space and time after a quantum quench in the Bose-Hubbard model. We derive equations of motion for the single-particle Green's function within the contour-time formalism, allowing us to study dynamics in the strong-coupling regime. We discuss the numerical solutions of these equations and calculate the single-particle density matrix for quenches in the Mott phase. We demonstrate light-cone-like spreading of correlations in the Mott phase in one, two, and three dimensions and calculate the propagation velocities in each dimension.

DOI: [10.1103/PhysRevA.98.053618](https://doi.org/10.1103/PhysRevA.98.053618)

## I. INTRODUCTION

The out-of-equilibrium dynamics of interacting quantum systems has become a major subject of interest in many-body physics. Experimental advances have made ultracold atoms in optical lattices a favorable setting for the study of out-of-equilibrium phenomena and attracted considerable attention in recent years [1–6]. These systems are highly versatile in that experimental parameters can be tuned over a wide range of values in real time. This facilitates the study of quantum quenches, in which parameters in the corresponding Hamiltonian are varied in time more rapidly than the system can respond adiabatically. Such protocols open the door to a rich range of many-body physics and have been studied intensely both theoretically and experimentally.

Jaksch *et al.* [7] showed that ultracold bosons trapped in optical lattices can be described by the Bose-Hubbard model (BHM)—a minimal model of interacting bosons on a lattice. The BHM exhibits a quantum phase transition between a superfluid and a Mott insulator as the ratio of the hopping strength,  $J$ , to the on-site interaction strength,  $U$ , is varied [8], which was demonstrated experimentally for cold atoms by Greiner *et al.* [9]. This allows for the study of quantum quenches across a quantum critical point, in addition to quenches within a particular phase.

A variety of quench protocols have been suggested and implemented [9–12] for the BHM in order to study out-of-equilibrium phenomena such as the Kibble-Zurek effect [10,13–15] and relaxation after a quench [16–32]. Our particular interest here is the light-cone-like spreading of correlations after a quantum quench. Several analytical and numerical studies have shown a Lieb-Robinson-like [33] maximal propagation velocity for the spreading of density correlations in one-dimensional systems for quenches from the superfluid-to-Mott-insulating regime as well as quenches solely within the superfluid [34] or Mott-insulating regimes

[20,27,35–37]. The latter case was recently observed by Cheneau *et al.* [38] for an array of decoupled one-dimensional chains. Some theoretical predictions have also been made for higher-dimensional systems [28,34,37,39] but these have not yet faced experimental scrutiny.

A generic problem in the theoretical description of quantum quenches is that it is necessary to have a formalism that is able to describe the physics in a broad area of parameter space. In the case of the BHM, numerical approaches such as exact diagonalization (ED) and the time-dependent density matrix renormalization group (t-DMRG) [16,17,27,29,35,36,38,40] can be essentially exact in all parts of parameter space but are limited by the system size and usually are practical only in one dimension. For dimensions higher than 1, methods such as time-dependent Gutzwiller mean-field theory [4,26,30,41] and dynamical mean-field theory [23] have been used, which can capture the presence of a quantum phase transition but, in their simplest form, do not capture spatial correlations. However, there has been work on including perturbative corrections [31,32,37,39,42–44] to remedy this weakness.

In previous work [45], we developed a real-time two-particle irreducible (2PI) effective action approach to the BHM based on a strong-coupling theory of the BHM [22,46] that is exact in both the weak- and the strong-coupling limits. We verified that by using a Hartree-Fock-Bogoliubov (HFB) approximation we were able to obtain considerable improvements beyond mean-field theory in calculating equilibrium properties of the BHM [45]. We also derived equations of motion for the single-particle Green's function using the contour-time formalism [47]. In this paper we use the equations of motion to investigate the case of a quench in the Mott-insulating regime. We demonstrate light-cone spreading of single-particle correlations in one, two, and three dimensions. We also study the dependence of the maximal propagation velocity on the quench protocol, chemical potential, temperature, and dimensionality, which should be relevant for comparisons with experiment.

The paper is structured as follows. In Sec. II, we describe the model that we study and the theoretical formalism we use to calculate correlations after a quench. In Sec. III, we

\*mrfitzpa@sfu.ca

†malcolmk@sfu.ca

briefly discuss the equations of motion for the single-particle Green's function that we obtained in our previous work [45] and show how they simplify for quenches that are confined to the Mott regime. In Sec. IV, we present numerical results obtained from integrating the equations of motion, and finally, in Sec. V, we discuss our results and present our conclusions.

## II. MODEL AND FORMALISM

In this section we introduce the Bose-Hubbard model and the effective theory (ET) we use to study quench dynamics in the strong-coupling regime, all within the context of the contour-time formalism. The Hamiltonian for the BHM, allowing for a time-dependent hopping term, is

$$\hat{H}_{\text{BHM}}(t) = \hat{H}_J(t) + \hat{H}_0, \quad (1)$$

where

$$\hat{H}_J(t) = - \sum_{\langle \vec{r}_1, \vec{r}_2 \rangle} J_{\vec{r}_1 \vec{r}_2}(t) (\hat{a}_{\vec{r}_1}^\dagger \hat{a}_{\vec{r}_2} + \hat{a}_{\vec{r}_2}^\dagger \hat{a}_{\vec{r}_1}) \quad (2)$$

and

$$\hat{H}_0 = \hat{H}_U - \mu \hat{N} = \frac{U}{2} \sum_{\vec{r}} \hat{n}_{\vec{r}} (\hat{n}_{\vec{r}} - 1) - \mu \sum_{\vec{r}} \hat{n}_{\vec{r}}, \quad (3)$$

with  $\hat{a}_{\vec{r}}^\dagger$  and  $\hat{a}_{\vec{r}}$  annihilation and creation operators for bosons at lattice site  $\vec{r}$ , respectively,  $\hat{n}_{\vec{r}} \equiv \hat{a}_{\vec{r}}^\dagger \hat{a}_{\vec{r}}$  the number operator,  $U$  the interaction strength, and  $\mu$  the chemical potential. The notation  $\langle \vec{r}_1, \vec{r}_2 \rangle$  indicates a sum over nearest neighbors only. We allow  $J_{\vec{r}_1 \vec{r}_2}(t)$ , the hopping amplitude between site  $\vec{r}_1$  and site  $\vec{r}_2$ , to be time dependent. We have specified the model for a uniform lattice but could consider a trap as used in experiments by introducing a site-dependent chemical potential. This leads to more complicated calculations than we consider here but is conceptually straightforward to include.

### A. Contour-time formalism

The general formalism that we discuss and adopt in this paper was developed in a previous paper of ours; we refer the reader to Ref. [45] for details on the formalism. We use the contour-time formalism [48–53], which treats time as a complex variable lying along a contour in a way that allows the description of out-of-equilibrium and equilibrium quantum phenomena within the same formalism. For systems initially prepared in thermal states, which we consider here, one can work with a contour  $C$  of the form illustrated in Fig. 1, which is sometimes referred to as the Konstantinov and Perel' (KP) contour [47]. A popular alternative to the KP contour is the Schwinger-Keldysh (SK) closed-time path [48,49], which is also suitable for initially thermalized systems. However, unlike the KP contour, the SK contour ignores transient phenomena, being more suitable for calculating steady states or other long-time phenomena. Given that transient effects are important in the spreading of space-time correlations after a quantum quench, the KP contour is a more appropriate choice. A number of authors have applied contour-time approaches to the BHM in out-of-equilibrium scenarios [22,23,45,54–64]. Similarly to Refs. [23], [45], and [55], we use an ET that arises from a contour approach suitable for strong and weak coupling but focusing on the spreading of correlations.

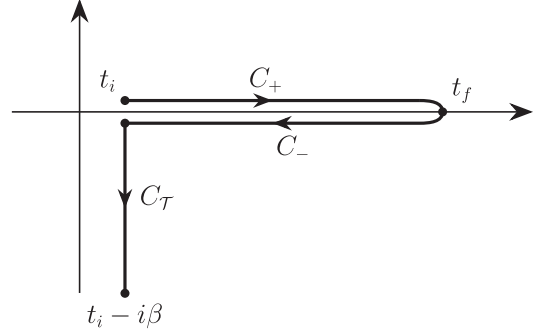


FIG. 1. Contour for a system initially prepared at time  $t_i$  in a thermal state with inverse temperature  $\beta$ .  $t_f$  is the maximum real time considered in the problem, which may be set to  $t_f \rightarrow \infty$  without loss of generality.

In our work, we develop an approach that is appropriate for strong and weak coupling that goes beyond previous work using the KP formalism [23] by including spatial fluctuations.

### B. Contour-ordered Green's functions

To characterize spatiotemporal correlations in the BHM we calculate contour-ordered Green's functions (COGFs). We define the  $n$ -point COGF as [53]

$$\begin{aligned} G_{\vec{r}_1 \dots \vec{r}_n}^{a_1 \dots a_n}(\tau_1, \dots, \tau_n) &\equiv (-i)^{n-1} \text{Tr} \{ \hat{\rho}_i T_C [\hat{a}_{\vec{r}_1}^{a_1}(\tau_1) \dots \hat{a}_{\vec{r}_n}^{a_n}(\tau_n)] \} \\ &\equiv (-i)^{n-1} \langle T_C [\hat{a}_{\vec{r}_1}^{a_1}(\tau_1) \dots \hat{a}_{\vec{r}_n}^{a_n}(\tau_n)] \rangle_{\hat{\rho}_i}, \end{aligned} \quad (4)$$

where  $\hat{\rho}_i$  is the state operator for a thermal state representing the initial state of our system,

$$\hat{\rho}_i = \frac{e^{-\beta \hat{H}_{\text{BHM}}(t_i)}}{\text{Tr} \{ e^{-\beta \hat{H}_{\text{BHM}}(t_i)} \}}, \quad (5)$$

the  $a_i$  upper indices are defined such that

$$\hat{a}_{\vec{r}}^1 \equiv \hat{a}_{\vec{r}}, \quad \hat{a}_{\vec{r}}^2 \equiv \hat{a}_{\vec{r}}^\dagger, \quad (6)$$

and  $\hat{a}_{\vec{r}}^a(\tau)$  are the bosonic fields in the Heisenberg picture with respect to  $\hat{H}_{\text{BHM}}(\tau)$  [Eq. (1)]:

$$\hat{a}_{\vec{r}}^a(\tau) = U^\dagger(\tau, \tau_i) \hat{a}_{\vec{r}}^a U(\tau, \tau_i), \quad (7)$$

$$U(\tau, \tau') = T_C [e^{-\int_{C(\tau, \tau')} dt \hat{H}_{\text{BHM}}(t)}]. \quad (8)$$

Here we have introduced explicitly the complex contour time argument  $\tau$ , the subcontour  $C(\tau, \tau')$ , which goes from  $\tau$  to  $\tau'$  along contour  $C$ , and the contour time ordering operator  $T_C$ , which orders strings of operators according to their position on the contour, with operators at earlier contour times placed to the right.

### C. Effective theory for the Bose-Hubbard model

In order to study quench dynamics in the BHM, we make use of an ET (expressed as an action) that can describe both the weak- and the strong-coupling limits of the model in the same formalism. Such an approach was developed in imaginary time by Sengupta and Dupuis [46] by using

two Hubbard-Stratonovich transformations, then generalized to the SK contour in Ref. [22], and then further generalized to the KP contour in Ref. [45] in conjunction with a 2PI effective action approach. A similar real-time theory was also obtained based on a Ginzburg-Landau approach using the Schwinger-Keldysh technique [56–58] in conjunction with a one-particle irreducible (1PI) effective action approach. In obtaining the ET below, one assumes that the system is dominated by the low-energy degrees of freedom, which is valid as long as the quench is sufficiently slow. A detailed discussion of the development of the effective theory within the KP contour formalism is presented in Ref. [45]. The ET obtained in Ref. [45] for  $z$  fields (which are obtained after two Hubbard-Stratonovich transformations and have the same correlations as the original  $a$  fields [46]) is

$$\begin{aligned}
 S[z] = & \frac{1}{2!} \sum_{\vec{r}} \int_C \int_C d\tau_1 d\tau_2 [\mathcal{G}^{-1}]^{a_1 a_2}(\tau_1, \tau_2) z_{\vec{r}}^{\bar{a}_1}(\tau_1) z_{\vec{r}}^{\bar{a}_2}(\tau_2) \\
 & + \frac{1}{2!} \sum_{\vec{r}_1 \vec{r}_2} \int_C d\tau \{2J_{\vec{r}_1 \vec{r}_2}(\tau) + \delta_{\vec{r}_1 \vec{r}_2} v_1\} \sigma_1^{a_1 a_2} z_{\vec{r}_1}^{\bar{a}_1}(\tau) z_{\vec{r}_2}^{\bar{a}_2}(\tau) \\
 & + \frac{1}{4!} \sum_{\vec{r}} \int_C d\tau \{-2u_1\} \sigma^{a_1 a_2 a_3 a_4} z_{\vec{r}}^{\bar{a}_1}(\tau) z_{\vec{r}}^{\bar{a}_2}(\tau) \\
 & \times z_{\vec{r}}^{\bar{a}_3}(\tau) z_{\vec{r}}^{\bar{a}_4}(\tau), \quad (9)
 \end{aligned}$$

where  $\mathcal{G}^{a_1 a_2}(\tau_1, \tau_2)$  is the atomic (i.e.,  $J = 0$ ) two-point Green's function (see Appendix C in Ref. [45] for the full expression),  $u_1$  is a time-independent quantity that is a complicated function of the inverse temperature  $\beta$  and the chemical potential  $\mu$  (see Appendix D in Ref. [45] for the full expression), and

$$v_1 = (2n_{J=0} + 1)u_1, \quad (10)$$

where  $n_{J=0}$  is the average particle density in the atomic limit. This can be calculated from the atomic kinetic Green's function  $\mathcal{G}^{12, (K)}$  (see Appendix C in Ref. [45]) as follows:

$$n_{J=0} = \frac{1}{2} \{i\mathcal{G}^{12, (K)}(t' = 0) - 1\}. \quad (11)$$

The overscored index  $\bar{a}$  used in Eq. (9) is defined by

$$f_{\vec{r}}^{\bar{a}}(\tau) \equiv \sigma_1^{a a'} f_{\vec{r}}^{a'}(\tau), \quad (12)$$

where  $\sigma_i$  is the  $i^{\text{th}}$  Pauli matrix, i.e.,  $\bar{1} = 2$  and  $\bar{2} = 1$ , and

$$\sigma^{a_1 a_2 a_3 a_4} \equiv \begin{cases} 1 & \text{if } \{a_m\}_{m=1}^4 \in P(\{1, 1, 2, 2\}), \\ 0 & \text{otherwise.} \end{cases} \quad (13)$$

We use the Einstein summation convention for the Nambu indices; i.e., matching indices implies a summation over all possible values of those indices.

When applied to an n PI effective action approach, where one ultimately calculates equations of motion for various correlation functions, the ET generates “anomalous” Feynman diagrams [22,45,46,65,66]. These diagrams contain internal inverse atomic propagator lines which do not correspond to any physical processes. If one considers all orders of the theory, they can be dropped because the different anomalous terms cancel. If the theory is truncated (as is usually the case), then care is required to ensure cancellation order by order. At

the level considered here, the  $v_1$  term in Eq. (9) plays this role. For a more detailed discussion of the cancellation of anomalous diagrams, see Ref. [45].

The effective theory introduces an effective potential  $v_1$  and a renormalized on-site interaction strength  $u_1$ . Moreover, it reassigns the role of the “bare propagator” to the atomic propagator. The theory gives the exact two-point connected COGF (CCOGF) in both the atomic and the noninteracting limits, thus making it particularly appealing for the study of quench dynamics since it gives a reasonable description of the behavior of the system in both the superfluid and the Mott-insulating regimes [6].

### III. EQUATIONS OF MOTION

Our goal is to calculate the full two-point CCOGF (henceforth the “full propagator”) after a quench, which encodes nonlocal single-particle spatial and temporal correlations. To achieve this, we solve Dyson's equation [45,67] for the full propagator (the superscript “c” indicates that  $G$  is a connected COGF),

$$\begin{aligned}
 G_{\vec{k}}^{a_1 a_2, c}(\tau_1, \tau_2) \equiv & [G_0]_{\vec{k}}^{a_1 a_2, c}(\tau_1, \tau_2) + \int_C \int_C d\tau_3 d\tau_4 [G_0]_{\vec{k}}^{a_1 a_3, c} \\
 & \times (\tau_1, \tau_3) \Sigma_{\vec{k}}^{\bar{a}_3 \bar{a}_4}(\tau_3, \tau_4) G_{\vec{k}}^{a_4 a_2, c}(\tau_4, \tau_2), \quad (14)
 \end{aligned}$$

where  $G_0$  is the bare propagator and  $\Sigma$  is the self-energy of the theory. Since we consider a translationally invariant system, we work in quasimomentum space rather than real space. In Ref. [45], we calculated the self-energy for the ET [Eq. (9)] in a systematic way using a 2PI effective action approach [67] and considered terms up to first order in  $u_1$  (loosely corresponding to an HFB-like approximation).

The equations of motion derived in Ref. [45] are quite general in that they can be applied to a variety of quench protocols. Here we consider the case in which the hopping quench is restricted to the Mott-insulating regime and the system is initially thermalized in the atomic limit. Under these conditions, the self-energy (and thus the equations of motion) simplify considerably, and it is straightforward to show that the equations of motion derived in Ref. [45] reduce to

$$A_{\vec{k}}(t, t') = \mathcal{A}(t - t') - i \int_{t'}^t dt'' \mathcal{A}(t - t'') \Sigma_{\vec{k}}^{(\text{HFB})}(t'') A_{\vec{k}}(t'', t'), \quad (15)$$

$$\begin{aligned}
 G_{\vec{k}}^{(K)}(t, t') = & \mathcal{G}^{(K)}(t - t') - i \int_0^t dt'' \mathcal{A}(t - t'') \Sigma_{\vec{k}}^{(\text{HFB})}(t'') \\
 & \times G_{\vec{k}}^{(K)}(t'', t') + i \int_0^{t'} dt'' \mathcal{G}^{(K)}(t - t'') \\
 & \times \Sigma_{\vec{k}}^{(\text{HFB})}(t'') A_{\vec{k}}(t'', t'), \quad (16)
 \end{aligned}$$

where  $A_{\vec{k}}(t, t')$  is the spectral function,

$$A_{\vec{k}}(t, t') = \langle \hat{a}_{\vec{k}}(t) \hat{a}_{\vec{k}}^\dagger(t') - \hat{a}_{\vec{k}}^\dagger(t') \hat{a}_{\vec{k}}(t) \rangle_{\hat{\rho}_i}, \quad (17)$$

and  $G_{\vec{k}}^{(K)}(t, t')$  is the kinetic Green's function,

$$\begin{aligned} G_{\vec{k}}^{(K)}(t, t') &= G_{\vec{k}}^{12, (K)}(t, t') \\ &= -i \langle \hat{a}_{\vec{k}}(t) \hat{a}_{\vec{k}}^\dagger(t') + \hat{a}_{\vec{k}}^\dagger(t') \hat{a}_{\vec{k}}(t) \rangle_{\hat{\rho}_i}. \end{aligned} \quad (18)$$

The quantities  $\mathcal{A}(t - t')$  and  $\mathcal{G}^{(K)}(t - t')$  that enter Eqs. (15) and (16) are the spectral function in the atomic limit and the kinetic Green's function in the atomic limit, respectively. In this limit both quantities are time translational invariant.  $\Sigma_{\vec{k}}^{(\text{HFB})}(t)$  is the self-energy in the HFB approximation,

$$\Sigma_{\vec{k}}^{(\text{HFB})}(t) = \epsilon_{\vec{k}}(t) + 2u_1 \{n(t) - n_{J=0}\}, \quad (19)$$

with

$$\epsilon_{\vec{k}}(t) = -2J(t) \sum_{i=1}^d \cos(k_i a), \quad (20)$$

$$n(t) = \frac{1}{N_{\text{sites}}} \sum_{\vec{k}} n_{\vec{k}}(t), \quad (21)$$

$$n_{\vec{k}}(t) = \frac{1}{2} \{i G_{\vec{k}}^{(K)}(t, t) - 1\}, \quad (22)$$

and  $a$  the lattice constant (assuming a  $d$ -dimensional hypercube geometry). In the atomic limit, the spectral function and kinetic Green's functions can be written as

$$\begin{aligned} \mathcal{A}(t) &= \frac{1}{\mathcal{Z}} \sum_{n=0}^{\infty} e^{-\beta(\mathcal{E}_n - \mathcal{E}_{n_{\text{MI}}})} \{ (n+1) e^{-i(\mathcal{E}_{n+1} - \mathcal{E}_n)t} \\ &\quad - n e^{i(\mathcal{E}_{n-1} - \mathcal{E}_n)t} \}, \end{aligned} \quad (23)$$

$$\begin{aligned} \mathcal{G}^{(K)}(t) &= -\frac{i}{\mathcal{Z}} \sum_{n=0}^{\infty} e^{-\beta(\mathcal{E}_n - \mathcal{E}_{n_{\text{MI}}})} \{ (n+1) e^{-i(\mathcal{E}_{n+1} - \mathcal{E}_n)t} \\ &\quad + n e^{i(\mathcal{E}_{n-1} - \mathcal{E}_n)t} \}, \end{aligned} \quad (24)$$

where  $\mathcal{E}_n$  is the single-site energy,

$$\mathcal{E}_n = \frac{U}{2} n(n-1) - \mu n, \quad (25)$$

$n_{\text{MI}}$  is the zero-temperature particle density,

$$n_{\text{MI}} = \lceil \mu/U \rceil, \quad (26)$$

and  $\mathcal{Z}$  is the partition function,

$$\mathcal{Z} = \sum_{n=0}^{\infty} e^{-\beta(\mathcal{E}_n - \mathcal{E}_{n_{\text{MI}}})}. \quad (27)$$

It is noteworthy that the equations of motion, (23) and (24), do not contain time integrals over imaginary time, even though we work with the KP contour (Fig. 1). This is because, in our ET, the self-energy  $\Sigma_{\vec{k}}^{a_1 a_2}(\tau_1, \tau_2)$  vanishes if either  $\tau_1$  or  $\tau_2$  lies on the imaginary part of the contour if the system is initially thermalized in the atomic limit (see Eqs. (93) and (94) in Ref. [45]). It is important to stress, however, that the equations of motion above still contain information about the initial thermal state through the bare propagator [Eqs. (23) and (24)], which is a function of the initial temperature.

We consider quenches in which the hopping amplitude  $J(t)$  is tuned as a function of time. (Experimentally, this corresponds to varying the depth of the optical lattice, since hopping varies exponentially with the lattice depth while interactions vary weakly with the lattice depth [68].) We choose  $J(t)$  to have the form

$$J(t) = \left( \frac{J_f - J_i}{2} \right) \tanh \left( \frac{t - t_c}{\tau_Q} \right) + \left( \frac{J_f + J_i}{2} \right), \quad (28)$$

which corresponds to the experimental scenario of a linear ramp. Note that  $\lim_{t \rightarrow -\infty} J(t) = J_i$ , and  $\lim_{t \rightarrow \infty} J(t) = J_f$ . The time scale  $\tau_Q$  is the characteristic time for  $J(t)$  to cross from  $J_i$  to  $J_f$ , and  $t_c$  is the time at which the middle of the quench occurs. Other forms of  $J(t)$  which are not linear may lead to differing behavior in the long-time limit [69]. For the quench scenario we consider in this paper,  $J_c > J_f > J_i = 0$ , where  $J_c$  is the critical hopping strength at the superfluid-to-Mott-insulator phase boundary (for fixed  $\mu$ ).

#### IV. NUMERICAL RESULTS

The equations of motion, Eqs. (15) and (16), form a system of nonlinear Volterra integral equations that have no known analytical solution, hence we take a numerical approach to solve them. This presents more of a challenge than the one-particle-irreducible equations of motion obtained in Ref. [22] due to the presence of memory kernels that incorporate the entire history of the system, making explicit the importance of the quench protocol to the postquench state. An additional important feature of the equations of motion is that they are causal, i.e., all quantities at some later time  $t_f$  can be obtained by integration over the known functions for times  $t \leq t_f$ . We exploit this feature of the equations to develop an implicit block-by-block scheme, closely following Ref. [70]. A detailed discussion of our numerical scheme is presented in Appendix A.

In this section we first compare the results of the solutions of Eqs. (15) and (16) to ED calculations. Obtaining acceptable agreement we then present numerical results for the light-cone-like propagation of single-particle spatial correlations in one, two, and three dimensions for quenches in the Mott-insulating regime.

##### A. Comparison to exact diagonalization calculations

First, we assess the accuracy of our ET by comparing calculations of the single-particle density matrix  $\rho_1(\Delta\vec{r}, t)$  obtained from this theory to ED calculations for small system sizes.  $\rho_1(\Delta\vec{r}, t)$  is a natural quantity for the study of single-particle spatial correlations, which can be calculated from the equal-time kinetic Green's function  $G_{\vec{k}}^{(K)}(t, t)$  as

$$\begin{aligned} \rho_1(\Delta\vec{r}, t) &= \frac{1}{N_s} \sum_{\vec{k}} \cos(\vec{k} \cdot \Delta\vec{r}) n_{\vec{k}}(t) \\ &= \frac{1}{2N_s} \sum_{\vec{k}} \cos(\vec{k} \cdot \Delta\vec{r}) \{i G_{\vec{k}}^{(K)}(t, t) - 1\}, \end{aligned} \quad (29)$$

where  $N_s$  is the number of sites.



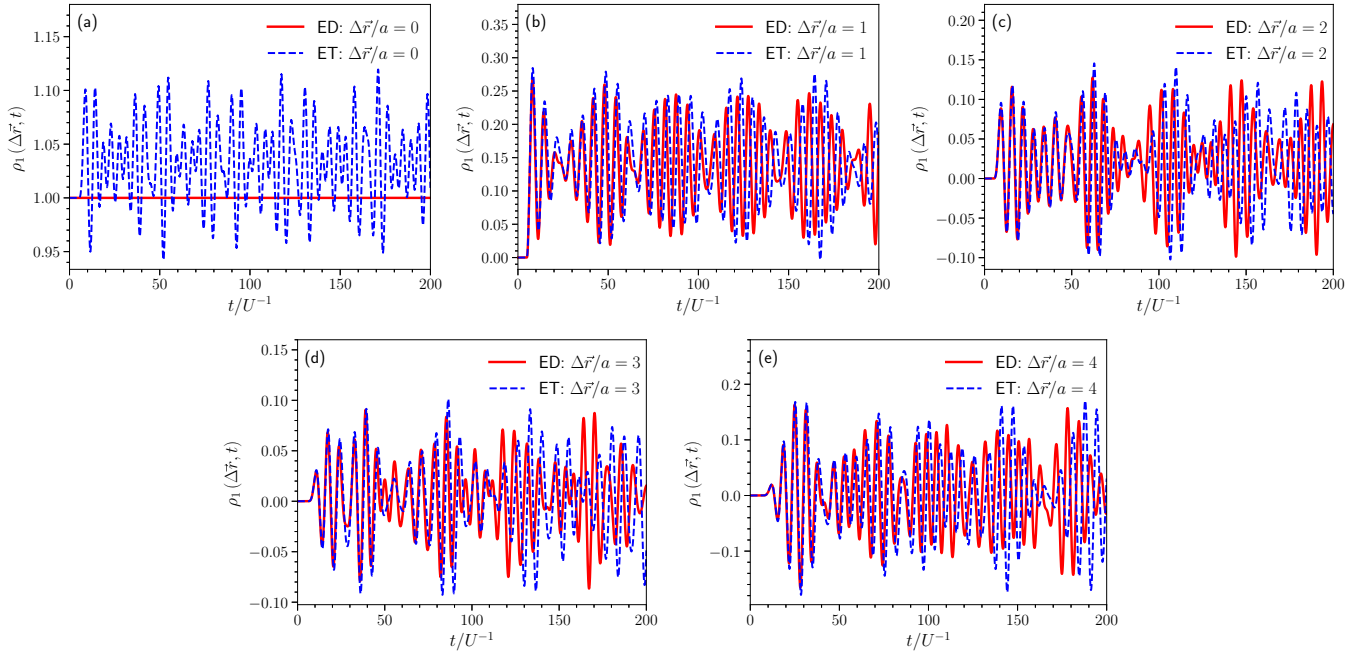


FIG. 2. Comparison of  $\rho_1(\Delta\vec{r}, t)$  obtained from our ET and from ED for (a)  $\Delta\vec{r}/a = 0$ , (b)  $\Delta\vec{r}/a = 1$ , (c)  $\Delta\vec{r}/a = 2$ , (d)  $\Delta\vec{r}/a = 3$ , and (e)  $\Delta\vec{r}/a = 4$ . The parameters are  $\beta U = \infty$ ,  $\mu/U = 0.4116$ ,  $J_f/U = 0.035$ ,  $t_c/U^{-1} = 5$ ,  $\tau_Q/U^{-1} = 0.1$ ,  $d = 1$ , and  $N_s = 8$ .

In Figs. 2 and 3, we display the time evolution of  $\rho_1(\Delta\vec{r}, t)$ , obtained from both the effective theory and ED, for a quench performed on an eight-site chain ( $d = 1$ ;  $N_s = 8$ ) with  $\beta = \infty$  ( $T = 0$ ),  $\mu/U = 0.4116$ ,  $t_c/U^{-1} = 5$ , and  $\tau_Q/U^{-1} = 0.1$ . The only parameter that differs between the two figures is the final hopping strength  $J_f/U$ , where  $J_f/U = 0.035$  for Fig. 2 and  $J_f/U = 0.05$  for Fig. 3.

Figure 2(a) shows  $\rho_1(\Delta\vec{r}, t)$  for  $\Delta\vec{r}/a = 0$ , which is equivalent to the average particle density. Figure 2(a) shows that our ET leads to small fluctuations in the particle number, typically of the order of 5%. In Appendix B, we discuss the origin of these particle number fluctuations. The results in Figs. 2(b)–2(e) show that this disagreement with ED is confined to  $\Delta\vec{r}/a = 0$  since for  $\Delta\vec{r}/a \neq 0$  our method is

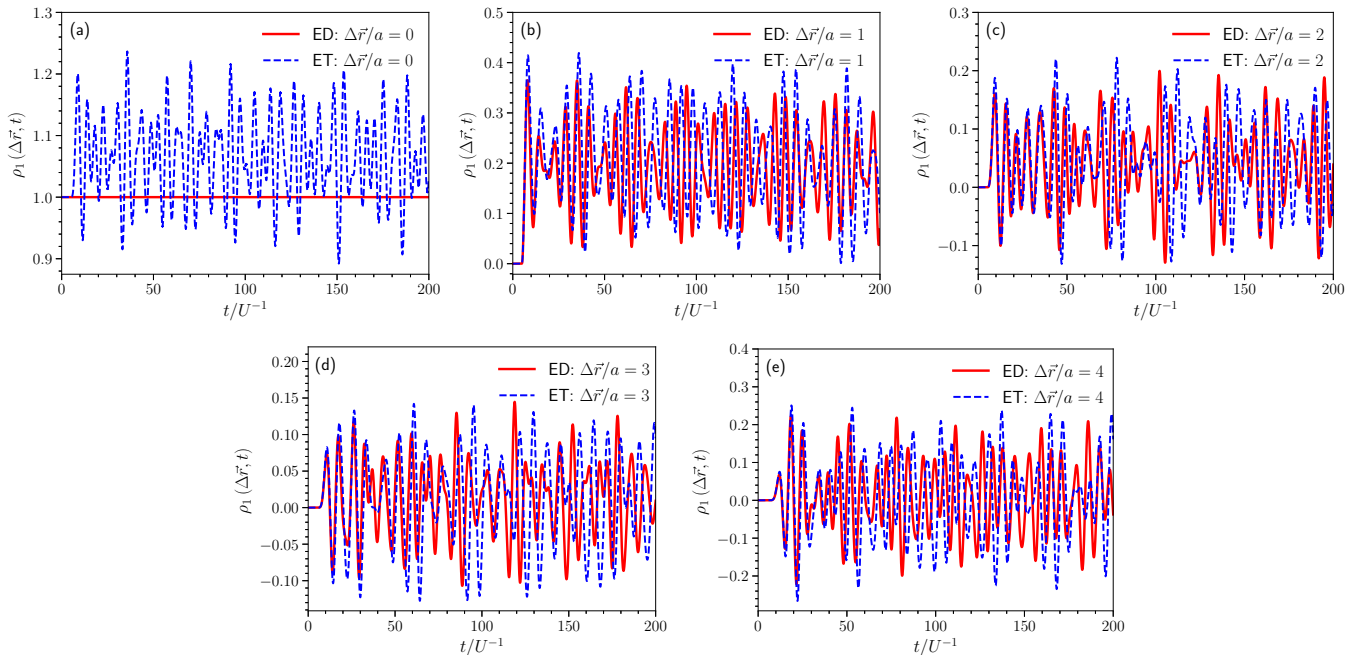


FIG. 3. Comparison of  $\rho_1(\Delta\vec{r}, t)$  obtained by our ET and by ED for (a)  $\Delta\vec{r}/a = 0$ , (b)  $\Delta\vec{r}/a = 1$ , (c)  $\Delta\vec{r}/a = 2$ , (d)  $\Delta\vec{r}/a = 3$ , and (e)  $\Delta\vec{r}/a = 4$ . The parameters are the same as in Fig. 2 except that  $J_f/U = 0.05$ .

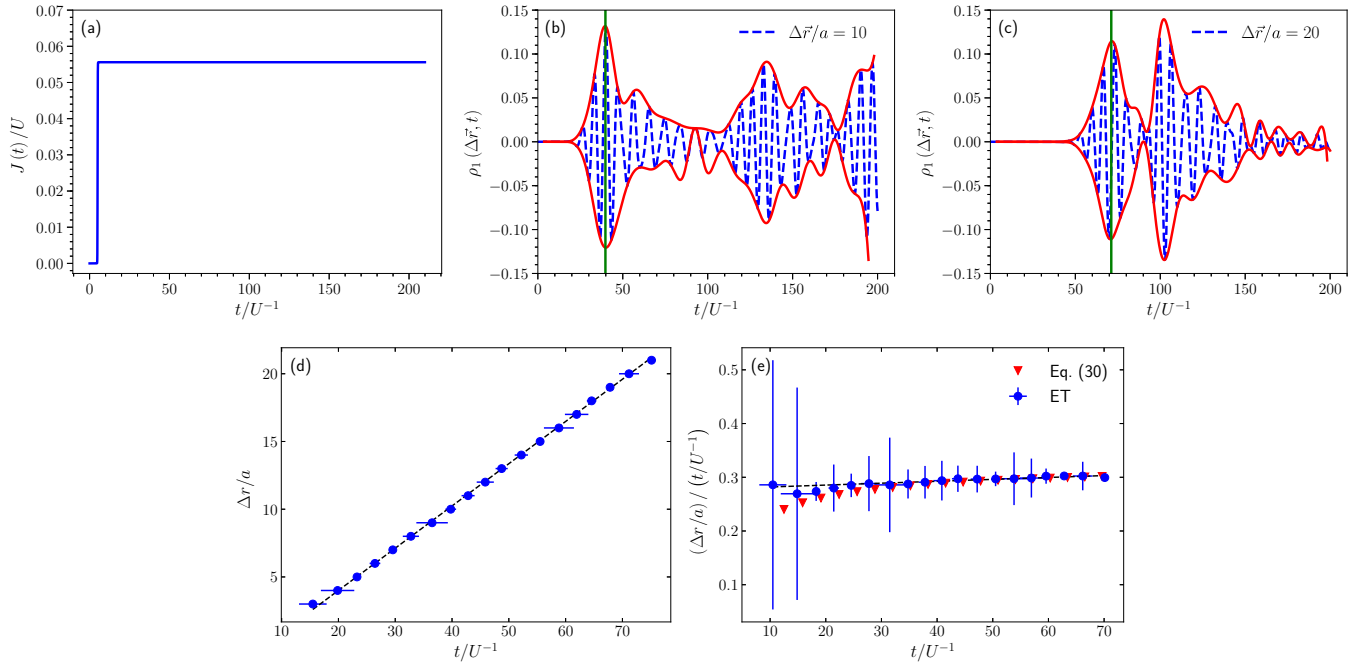


FIG. 4. (a) Evolution of  $J(t)/U$  for quench parameters  $J_f/U = 0.0556$ ,  $t_c/U^{-1} = 5$ , and  $\tau_Q/U^{-1} = 0.1$ ; (b) dynamics of  $\rho_1(\Delta\vec{r}, t)$  for  $\Delta\vec{r}/a = 10$ ; (c) dynamics of  $\rho_1(\Delta\vec{r}, t)$  for  $\Delta\vec{r}/a = 20$ ; (d) scatterplot of the time  $t/U^{-1}$  it takes for the single-particle correlation front to travel a distance  $\Delta r/a$ ; (e) scatterplot of  $(\Delta\vec{r}/a)/(t/U^{-1})$  vs  $t/U^{-1}$ , with a comparison to results obtained from Eq. (30). To directly compare our results with those obtained in Ref. [36] for (e), we shift our travel times by  $t_c$  such that  $t = 0$  corresponds to the middle of our (quasi-instantaneous) quench. We show a straight-line fit to the data in both (d) and (e). In (b) and (c), solid red lines trace the envelopes of the wavepackets, while the solid green vertical line estimates the position of the center of the first wavepacket. The parameters in (b)–(e) include the quench parameters in (a), as well as  $\mu/U = 0.4116$ ,  $\beta U = 1000$ ,  $d = 1$ , and  $N_s = 50$ .

quantitatively accurate for times up to  $\sim 100U^{-1}$ . At later times, the fast oscillations calculated by our method start to become out of phase with those obtained by ED.

Figures 3(a)–3(e) display the time evolution of  $\rho_1(\Delta\vec{r}, t)$  for a system identical to that shown in Figs. 2(a)–2(e) except that  $J_f/U = 0.05$ . For this value of  $J_f$ , the ET is quantitatively accurate for times up to  $\sim 50U^{-1}$  when  $\Delta\vec{r}/a \neq 0$ . This is a sufficiently long time window to allow the identification of the peak of the first wavepacket in  $\rho_1(\Delta\vec{r}, t)$  at a given  $\Delta\vec{r}/a \neq 0$ , which we use to determine the velocity at which single-particle correlations spread. The good agreement with ED results in eight-site systems gives us confidence in the results we obtain in larger systems and higher dimensions where comparison with ED is not possible.

### B. Light-cone spreading of single-particle spatial correlations

In this section, we demonstrate light-cone-like spreading [33] of single-particle correlations in one, two, and three dimensions, and we compare the velocities we obtain for the propagation of correlations to existing results in the field [27,28,32,35–39]. We performed calculations of the spreading of correlations in one (50-site chains), two ( $50 \times 50$  systems), and three ( $28 \times 28 \times 28$  systems) dimensions for a variety of model parameters and found light-cone-like spreading of correlations in all cases. Our results are in good agreement

with previously obtained exact results in one dimension [36]. We present our detailed results below.

#### 1. One dimension

Before presenting results for the velocity at which single-particle correlations spread, we first discuss how we identify this velocity. In Fig. 4(b), we display the time evolution of the single-particle correlation function  $\rho_1(\Delta\vec{r}, t)$  for a 50-site chain, with  $\Delta\vec{r}/a = 10$ . In this figure, we can see the emergence of multiple wavepackets after the quench. Solid red lines trace the envelopes of these wavepackets which we determine from an interpolation based on a fourth-order spline. The solid green vertical line represents our estimation of the center of the first wavepacket. In Fig. 4(c), where  $\Delta\vec{r}/a = 20$  one can see that the center of the first wavepacket is shifted to a later time, i.e., it takes a longer time for the single-particle correlations to spread out to larger particle separation distances  $\Delta r/a$ . To track the propagation of the single-particle correlations, we plot the particle separation displacement  $\Delta\vec{r}/a$  of the first wavepacket against time  $t/U^{-1}$ .

We do this for the above 50-site chain system in Fig. 4(d) and note that the data appear to be compatible with a linear fit, which would imply that there is a propagating front of single-particle correlations that travels through the one-dimensional chain at a constant velocity. When we plot  $(\Delta\vec{r}/a)/(t/U^{-1})$  on the y axis rather than  $\Delta\vec{r}/a$ , as we do in Fig. 4(e), we see that the velocity tends toward an asymptotic limit  $v_{\max}$ . Using

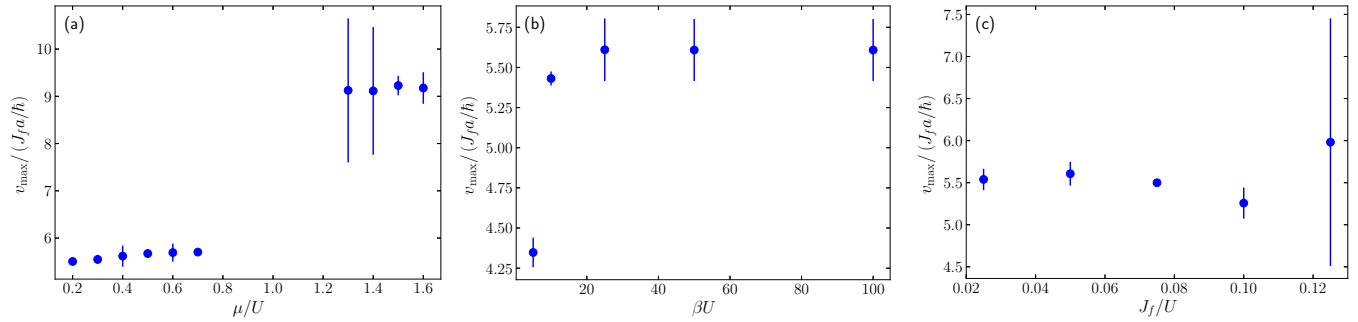


FIG. 5. Scatterplots of the propagation velocity  $v/(J_f a/\hbar)$  in one dimension as a function of various model parameters. In all cases  $t_c/U^{-1} = 5$  and  $\tau_Q/U^{-1} = 0.1$ . (a) Scatterplot of  $v/(J_f a/\hbar)$  as a function of  $\mu/U$  for a 50-site chain with  $\beta U = 1000$  and  $J_f/U = 0.0556$ ; (b) scatterplot of  $v/(J_f a/\hbar)$  as a function of  $\beta U$  for a 50-site chain with  $\mu/U = 0.4116$  and  $J_f/U = 0.0556$ ; (c) scatterplot of  $v/(J_f a/\hbar)$  as a function of  $J_f/U$  for a 50-site chain with  $\beta U = 1000$  and  $\mu/U = 0.4116$ .

an unconstrained fermionization procedure in one dimension, Barmettler *et al.* found the first correlation peak time  $t_{\text{peak}}$  to be approximated by [36]

$$\frac{t_{\text{peak}}}{U^{-1}} \approx \frac{1}{6} \left( \frac{J}{U} \right)^{-1} \left[ \frac{\Delta r}{a} + 1.02 \left( \frac{\Delta r}{2a} \right)^{1/3} \right], \quad (30)$$

which they showed agrees quantitatively with DMRG calculations for instantaneous quenches in the strong-coupling regime. For comparison, we plot Eq. (30) in Fig. 4(e) and find that there is good agreement with our results for larger  $\Delta r$ . In our calculation, the propagation velocity tends to its asymptotic limit sooner than that obtained in the fermionization procedure.

Performing a linear fit in Fig. 4(d) yields an estimate for the maximal velocity of  $v_{\text{max}} = (5.6 \pm 0.2) \frac{J_f a}{\hbar}$ , for this particular set of parameters. The authors of Ref. [36] obtained  $v_{\text{max}} \approx 5.7 \frac{J_f a}{\hbar}$  for the same parameters from a DMRG calculation, which our result agrees with to within error bars. It is noteworthy that the quoted velocity obtained using the DMRG in Ref. [36] is actually for the density-density correlation function, but within the approximations used in Ref. [36] the velocity obtained from the density-density correlation function matches that obtained from the single-particle correlation function. In our theory, these velocities only match in the infinite interaction limit, but because we work at strong coupling we expect that this distinction is unlikely to affect our results significantly.

In Fig. 5 we summarize our results for the maximal propagation velocity in one dimension as a function of the chemical potential, temperature, and  $J_f/U$  for a 50-site chain. We see that except at temperatures comparable to the melting temperature of the Mott insulator  $\beta U \sim 5$ , the velocities we extract all lie in the range  $5.5 J_f a/\hbar$  to  $6 J_f a/\hbar$  for  $0 < \mu/U < 1$  (or  $\bar{n} = 1$ ) and show little sensitivity to  $J_f/U$  or  $\mu/U$ . The velocity range we obtain for strong coupling is consistent with that obtained in Ref. [36], where they establish a velocity range between the two limiting cases of the BHM: for infinitely strong interactions in one dimension, they obtained a maximal velocity of  $v_{\text{max}} = 6 J a/\hbar$  for  $\bar{n} = 1$ , and in the limit of no interactions they obtained a value of  $v_{\text{max}} = 4 J_f a/\hbar$  for  $\bar{n} = 1$ . Moreover, the velocities we obtain exhibit the same bosonic enhancement with respect to the average particle density  $\bar{n}$  as found in Ref. [36], namely, that

(apart from very small corrections)

$$v_{\text{max}} \propto (2\bar{n} + 1). \quad (31)$$

The enhancement with  $\bar{n}$  can be seen in Fig. 5(a), where  $v_{\text{max}}^{\bar{n}=1} = (5.6 \pm 0.1) \frac{J_f a}{\hbar}$  for  $0 < \mu/U < 1$  and  $v_{\text{max}}^{\bar{n}=2} = (9.2 \pm 0.9) \frac{J_f a}{\hbar}$  for  $1 < \mu/U < 2$ , which yields a ratio of  $v_{\text{max}}^{\bar{n}=2}/v_{\text{max}}^{\bar{n}=1} = 1.6 \pm 0.1$ , in agreement with the expected ratio from Eq. (31) of  $5/3 \approx 1.66$  within uncertainties.

Experimental data on the spreading of density-density correlations also lie in the range  $5\text{--}6 J a/\hbar$  for quenches in the Mott regime [38]. A recent calculation of the spreading of density-density correlations in one dimension found a value of  $v_{\text{max}} = 3.7 J a/\hbar$  for weak interactions [28] and Krutitsky *et al.* [37] obtained an analytical estimate of  $v_{\text{max}} = 3 J_f a/\hbar$  for the single-particle density matrix by performing a perturbative expansion of the von Neumann equation with respect to the inverse coordination number,  $1/z$ , for small  $J_f$ .

## 2. Two dimensions

Snapshots of the spatial dependence of  $\rho_1(\Delta\vec{r}, t)$  at different moments in time for a  $50 \times 50$ -site system are shown in Fig. 6, where each pixel represents a different particle separation displacement  $\Delta\vec{r}/a$ , and  $\Delta\vec{r}/a = 0$  is in the middle of each panel. In this figure, we see that the propagation of the single-particle correlations is anisotropic, with the propagation velocity maximal along the diagonal and minimal along the crystal axes. Krutitsky *et al.* [37] found the same anisotropic spreading of single-particle correlations for a similar quench protocol. Anisotropic behavior was also observed by Carleo *et al.* [34] in the spreading of density-density correlations within the superfluid regime. However, they found that the propagation velocity was maximal along the crystal axes and minimal along the diagonal, opposite to the behavior observed here and in Ref. [37] for the Mott insulator.

We found acquiring estimates for the maximum propagation velocities in higher dimensions to be somewhat more difficult than in one dimension. This difficulty is illustrated in Fig. 7, where we extract the maximal propagation velocities along a crystal axis and the diagonal for the same  $50 \times 50$  system considered in Fig. 6. Figures 5(a) and 5(b) display the time evolution of  $\rho_1(\Delta\vec{r}, t)$  for  $\Delta\vec{r}/a = (8, 0)$  (i.e., along

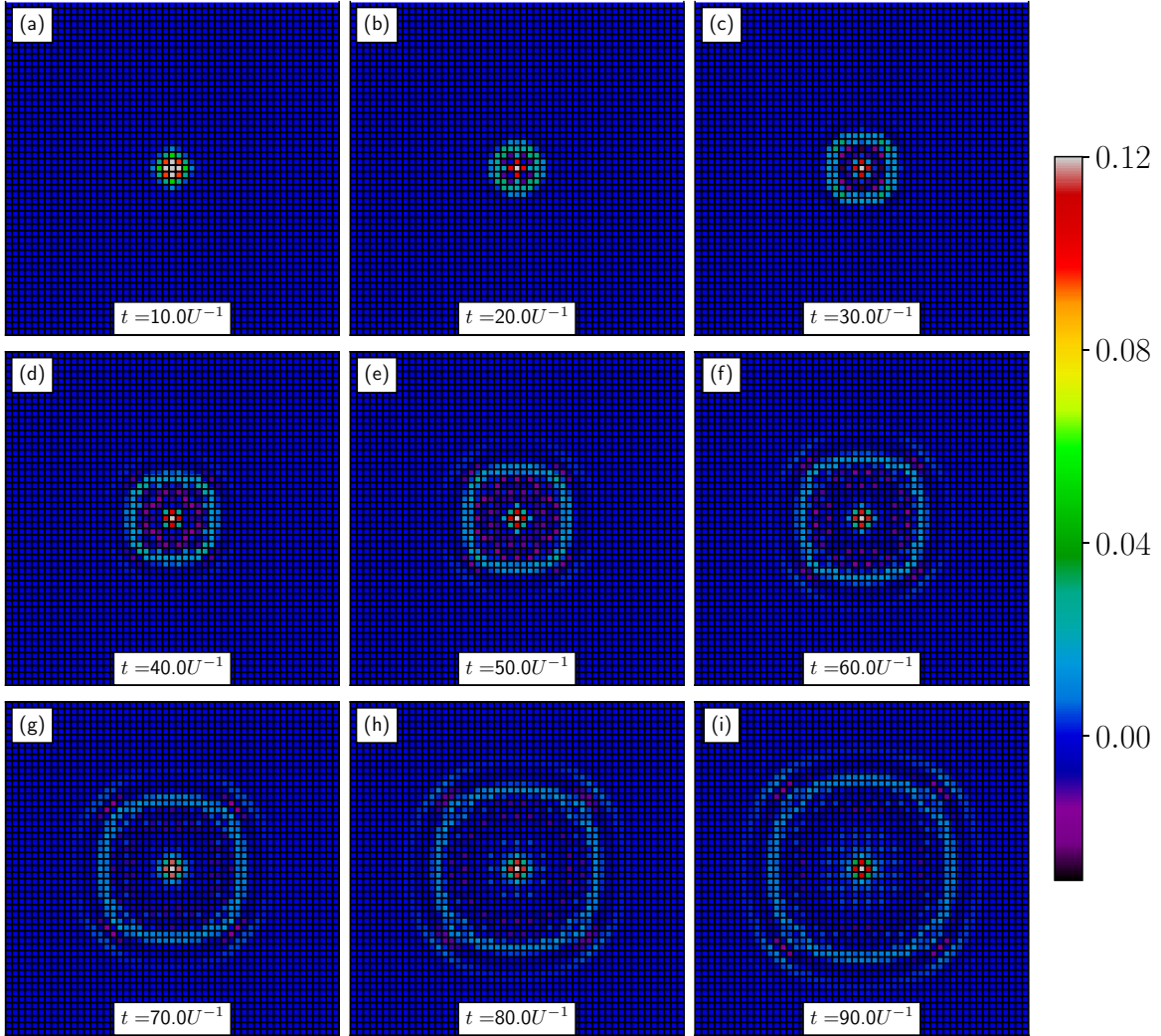


FIG. 6. Spatial dependency of  $\rho_1(\Delta\vec{r}, t)$  at different moments in time  $t/U^{-1}$  for a  $50 \times 50$ -site system. The parameters are  $\beta U = 1000$ ,  $\mu/U = 0.4136$ ,  $J_f/U = 0.025$ ,  $t_c/U^{-1} = 5$ , and  $\tau_Q/U^{-1} = 0.1$ .

a crystal axis) and  $\Delta\vec{r}/a = (8, 8)$  (i.e., along a diagonal), respectively. Upon comparing the two figures, we see that the wavepacket along the crystal axis is less sharp than that along the diagonal. Consequently, there is more uncertainty in our estimate of the center of a wavepacket (and hence the maximal propagation velocity) along a crystal axis than along a diagonal. This trend extends to three dimensions as well where the wavepackets are sharpest along the main diagonals, less sharp along the secondary diagonals, and even less sharp along the crystal axes. The linear fits in Figs. 7(c) and 7(d) yield the following maximal velocity estimates for  $J_f/U = 0.025$  of

$$v_{\max}^{(10)} = (6.8 \pm 0.3) \frac{J_f a}{\hbar}, \quad (32)$$

$$v_{\max}^{(11)} = (8.1 \pm 0.1) \frac{J_f a}{\hbar}, \quad (33)$$

where  $v_{\max}^{(10)}$  and  $v_{\max}^{(11)}$  are the maximal propagation velocities along the crystal axes and the diagonals, respectively.

Figures 8(a)–8(c) plot the maximal propagation velocities for a  $50 \times 50$  system as a function of  $\mu/U$ ,  $\beta U$ , and  $J_f/U$ ,

respectively, while keeping all the remaining parameters fixed. From Figs. 8(a) and 8(b), we see that the propagation velocities are not very sensitive to  $\mu$  (while remaining within the same Mott lobe) or to temperatures below the full melting of the Mott-insulating phase ( $\beta \gtrsim 5U$ ). In Fig. 8(c), we see that there appears to be a slight increase in the maximal propagation velocity and a decrease in the anisotropy for larger  $J_f/U$ . Extrapolating to larger values of  $J_f/U$  it seems plausible that there might be a value of  $J_f/U$  where the spreading of correlations becomes isotropic, especially given the results of Carleo *et al.* [34] in the superfluid regime, where they found the maximal propagation velocity to be along the crystal axes, not the diagonals. In future work, we plan to investigate quench protocols where one crosses the phase boundary into the superfluid regime, which will allow us to verify whether this is indeed the case. Technically this requires the inclusion of broken symmetry terms in the equations of motion since these terms are required for a full description of the superfluid regime.

In two dimensions, for  $0 < \mu/U < 1$ , the velocities  $v_{\max}^{(10)}$  we obtained along the crystal axes ranged from  $5.7 Ja/\hbar$  to  $7.6 Ja/\hbar$ , whereas the velocities  $v_{\max}^{(11)}$  along the



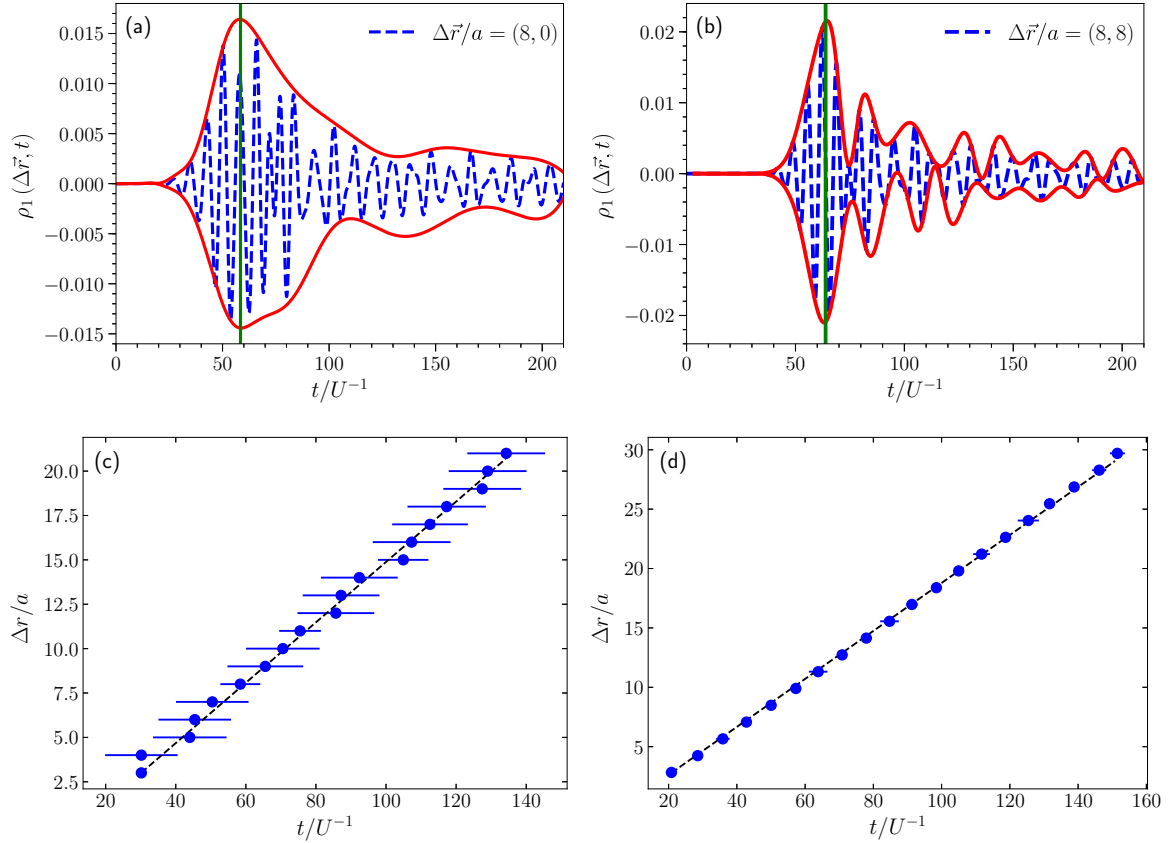


FIG. 7. Tracking the wavefront for a  $50 \times 50$ -site system. (a) Dynamics of  $\rho_1(\Delta\vec{r}, t)$  for  $\Delta\vec{r}/a = (8, 0)$ ; (b) dynamics of  $\rho_1(\Delta\vec{r}, t)$  for  $\Delta\vec{r}/a = (8, 8)$ ; (c) scatterplot of the time  $t/U^{-1}$  it takes for the single-particle correlation front to travel a distance  $\Delta r/a$  along a crystal axis; (d) scatterplot of the time  $t/U^{-1}$  it takes for the single-particle correlation front to travel a distance  $\Delta r/a$  along a diagonal. We show a straight-line fit to the data. In (b) and (c), solid red lines trace the envelopes of the wavepackets, while the solid green vertical line estimates the position of the center of the first wavepacket. The parameters in (a)–(d) are  $\mu/U = 0.4136$ ,  $\beta U = 1000$ ,  $J_f/U = 0.025$ ,  $t_c/U^{-1} = 5$ , and  $\tau_Q/U^{-1} = 0.1$ .

diagonal ranged from  $7.8 Ja/\hbar$  to  $8.7 Ja/\hbar$ . The only other related study that we are aware of is that by Krutitsky *et al.* [37], where they obtained analytical estimates of  $v_{\max}^{(10)} = 3Ja/\hbar$  and  $v_{\max}^{(11)} = 3\sqrt{2}Ja/\hbar$  for the crystal axes and diagonals, respectively. It is noteworthy that Krutitsky *et al.* also performed numerical calculations of the single-particle correlation spreading beyond their lowest-order analytical

calculations, however, they did not report any velocity estimates based on their numerical data. One prediction of Krutitsky *et al.* that does seem reasonably robust is the ratio  $v_{\max}^{(11)}/v_{\max}^{(10)}$ , for which their lowest-order estimate is  $\sqrt{2}$ . Examination of Fig. 8(c) shows that our results are consistent with  $v_{11}/v_{10} \simeq \sqrt{2}$  for small  $J_f/U$ , with the ratio decreasing with increasing  $J_f/U$ .

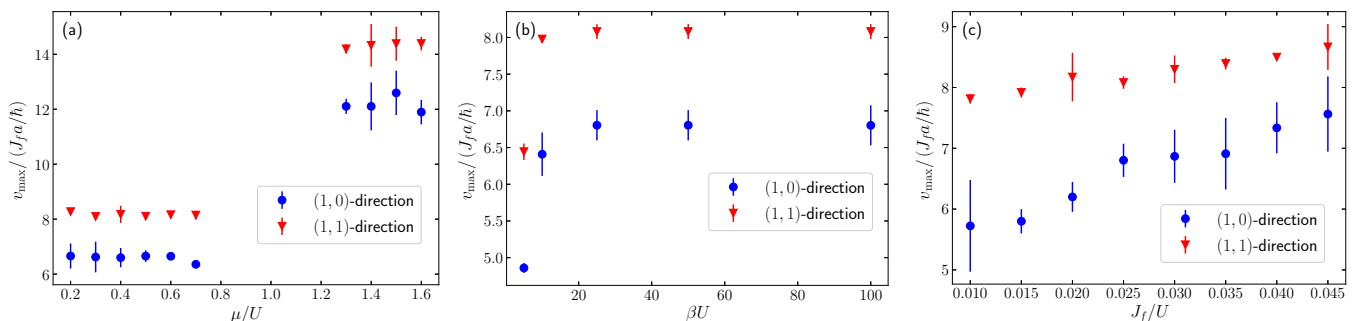


FIG. 8. Scatterplots of the propagation velocity  $v/(J_f a/\hbar)$  in two dimensions for a  $50 \times 50$ -site system as a function of various model parameters. In all cases  $t_c/U^{-1} = 5$  and  $\tau_Q/U^{-1} = 0.1$ . (a) Scatterplot of  $v/(J_f a/\hbar)$  as a function of  $\mu/U$  with  $\beta U = 1000$  and  $J_f/U = 0.025$ ; (b) scatterplot of  $v/(J_f a/\hbar)$  as a function of  $\beta U$  with  $\mu/U = 0.4136$  and  $J_f/U = 0.025$ ; (c) scatterplot of  $v/(J_f a/\hbar)$  as a function of  $J_f/U$  with  $\beta U = 1000$  and  $\mu/U = 0.4136$ .

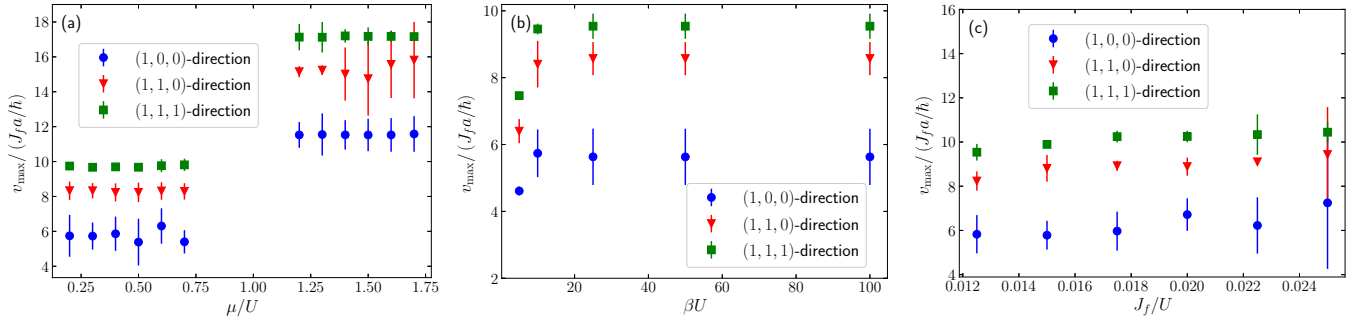


FIG. 9. Scatterplots of the propagation velocity  $v/(J_f a/\hbar)$  in three dimensions for a  $28 \times 28 \times 28$ -site system as a function of various model parameters. In all cases  $t_c/U^{-1} = 5$  and  $\tau_Q/U^{-1} = 0.1$ . (a) Scatterplot of  $v/(J_f a/\hbar)$  as a function of  $\mu/U$  with  $\beta U = 1000$  and  $J_f/U = 0.0125$ ; (b) scatterplot of  $v/(J_f a/\hbar)$  as a function of  $\beta U$  with  $\mu/U = 0.4132$  and  $J_f/U = 0.0125$ ; (c) scatterplot of  $v/(J_f a/\hbar)$  as a function of  $J_f/U$  with  $\beta U = 1000$  and  $\mu/U = 0.4132$ .

In higher dimensions, we find that the bosonic enhancement of the velocities as  $\bar{n}$  is increased is more pronounced than that in the one-dimensional case. From Fig. 8(a), we obtain  $v_{\max}^{\bar{n}=2}/v_{\max}^{\bar{n}=1} = 1.8 \pm 0.1$  along both the diagonals and the crystal axes. The behavior is qualitatively similar to that in one dimension, but we are not aware of any exact results in higher dimensions equivalent to Eq. (30) with which to compare our numerical results.

### 3. Three dimensions

We find similar behavior in three dimensions to that found in two dimensions, as displayed in Fig. 9, where we see that the velocity depends strongly on the crystal direction but is otherwise relatively insensitive to changes in the chemical potential (within the same Mott lobe), temperature, or final hopping value  $J_f$ . The trend towards increasing isotropy in the spread of correlations as  $J_f/U$  increases is much less pronounced than in two dimensions, perhaps because we consider smaller values of  $J_f$  than in two dimensions. Our work calculates the maximal propagation velocities for correlations in three dimensions for the BHM: for  $0 < \mu/U < 1$  we obtain  $v_{\max}^{(100)} \sim 6J_f a/\hbar$ ,  $v_{\max}^{(110)} \sim 8.5J_f a/\hbar$ , and  $v_{\max}^{(111)} \sim 10J_f a/\hbar$ ; and for  $1 < \mu/U < 2$  we obtain  $v_{\max}^{(100)} \sim 11.5J_f a/\hbar$ ,  $v_{\max}^{(110)} \sim 15.5J_f a/\hbar$ , and  $v_{\max}^{(111)} \sim 17J_f a/\hbar$ .

## V. DISCUSSION AND CONCLUSIONS

The ability to address single sites in cold-atom experiments [12] has allowed for experimental exploration of spatiotemporal correlations in the BHM [38]. This has led to theoretical investigations of these correlations in both one [36] and higher [28,32,34,37] dimensions in the presence of a quench. In dimensions higher than 1, where numerical approaches are limited, a theoretical challenge has been to develop a framework which can treat correlations in both the superfluid and the Mott-insulating phases over the course of a quench. In a previous paper [45], we developed a formalism that allows for such a description of the space and time dependence of single-particle correlations. The specific approach we took was to derive a 2PI effective action for the BHM using the KP contour, building on the 1PI real-time strong-coupling low-energy theory developed in Ref. [22], which generalizes the imaginary-time theory developed in Ref. [46]. From this 2PI

effective action we were able to derive equations of motion that treat the superfluid order parameter and the full two-point Green's functions on equal footing. One of the attractive features of the formalism is that it is applicable even in the limit of a low occupation number per site.

We used the formalism to study out-of-equilibrium dynamics, focusing on the light-cone-like spreading of single-particle correlations after a quench. We considered quenches in the Mott-insulator phase and solved the equations of motion for the single-particle density matrix  $\rho_1(\Delta\vec{r}, t)$ . From the calculation of  $\rho_1(\Delta\vec{r}, t)$ , we demonstrated light-cone-like spreading of single-particle correlations in one, two, and three dimensions. The range of maximal propagation velocities that we obtain in one dimension agree well with recent theoretical [36] and experimental [38] results over the range of parameter values we consider. In higher dimensions, we find that there is anisotropic spreading of correlations, where the propagation velocity is maximal along the main diagonal and minimal along the crystal axes. Similar anisotropic spreading of correlations was observed in calculations in Ref. [37]. We also observed that at least in two dimensions, the degree of anisotropy appears to diminish with increasing final hopping strength  $J_f$ . This raises the question whether the spreading becomes isotropic for  $J_f$  in the vicinity of  $J_c$ , particularly given that it has been predicted that in the superfluid regime the propagation velocity is maximal along the crystal axes, rather than the diagonals [34]. To address these questions within our formalism requires a more careful treatment of the equations of motion. One needs to include broken symmetry terms which become relevant upon entering the superfluid regime. We defer this task to future work.

The space and time dependence of correlations after a quantum quench give insight into the propagation of excitations generated by that quench, and hence we hope that the formalism we have developed here will allow further theoretical investigation of the excitations after quenches in the BHM, to complement experimental efforts in the same direction. In future work we plan to investigate a broader range of quench protocols and generalizations such as the inclusion of a harmonic trap, coupling to a bath [54,55,71], disorder [72–75], and multicomponent [76] Bose-Hubbard models.

### ACKNOWLEDGMENTS

This work was supported by NSERC.

### APPENDIX A: NUMERICAL IMPLEMENTATION OF THE SOLUTION OF THE EQUATIONS OF MOTION

In this Appendix, we describe in more detail the numerical implementation of the solutions to the equations of motion. We begin by rewriting Eqs. (15) and (16) in a slightly more compact form,

$$A_{\vec{k}}(t, t') = \mathcal{A}(t - t') + \int_{t'}^t dt'' K_{\vec{k}}^{(1)}(t, t'', n(t'')) A_{\vec{k}}(t'', t'), \quad (\text{A1})$$

$$G_{\vec{k}}^{(K)}(t, t') = \mathcal{G}^{(K)}(t - t') + \int_0^t dt'' K_{\vec{k}}^{(1)}(t, t'', n(t'')) G_{\vec{k}}^{(K)}(t'', t') + \int_0^{t'} dt'' K_{\vec{k}}^{(2)}(t, t'', n(t'')) A_{\vec{k}}(t'', t'), \quad (\text{A2})$$

where we define the kernels

$$K_{\vec{k}}^{(1)}(t, t'', n(t'')) = -i\mathcal{A}(t - t'') \Sigma_{\vec{k}}^{(\text{HFB})}(t''), \quad (\text{A3})$$

$$K_{\vec{k}}^{(2)}(t, t'', n(t'')) = i\mathcal{G}^{(K)}(t - t'') \Sigma_{\vec{k}}^{(\text{HFB})}(t''). \quad (\text{A4})$$

We include  $n(t'')$  in the kernel arguments to emphasize the fact that both kernels are functions of the particle density. The presence of  $n(t'')$  in the kernels couples the equations of motion for a fixed quasimomentum  $\vec{k}$  to the remaining equations (with different  $\vec{k}$ ) since  $n(t'')$  is calculated from  $\sum_{\vec{k}} G_{\vec{k}}^{(K)}(t'', t')$ . Moreover, for  $t \geq t'$ , the calculation of  $A_{\vec{k}}(t, t')$  and  $G_{\vec{k}}^{(K)}(t, t')$  depends on  $n(t)$ , not simply the history. These nonlinearities complicate the numerical solution, as we must resort to implicit methods. At a general level, the simplest method to solve such a nonlinear system is to apply a self-consistent approach, which we do in this paper. For each time step in  $t$ , we start by guessing the value of  $n(t)$ , then we solve each equation separately for values of  $t'$  in the range  $t \geq t' \geq 0$  using an explicit numerical approach, then we use our calculation of the  $G_{\vec{k}}^{(K)}(t, t')$  values to update  $n(t)$ , and then we repeat until we obtain convergence. Once convergence is achieved, we take another time step in  $t$ , then repeat the above procedure starting with  $t' = 0$  to  $t' = t$ . One can guess  $n(t)$  using the final value for  $n(t - \Delta t)$  or by doing an extrapolation based on several previous time steps.

After guessing and updating the value of  $n(t)$ , we implement a modified block-by-block algorithm based on that in Ref. [70]. The block-by-block method uses a combination of

Simpson's rule and Lagrange interpolation points to discretize the equations of motion in such a way as to generate a system of equations in terms of multiple unknowns that can then be solved simultaneously. For example, if we introduce the discretization notation

$$F_m = F(m\Delta t), \quad (\text{A5})$$

then for fixed  $m \geq m'$ , after applying the block-by-block procedure, we obtain a pair of simultaneous equations for  $[A_{\vec{k}}]_{2m+1, 2m'}$  and  $[A_{\vec{k}}]_{2m+2, 2m'}$ , a single equation for  $[A_{\vec{k}}]_{2m+1, 2m'+1}$ ,  $[A_{\vec{k}}]_{2m+2, 2m'+1}$ , and  $[A_{\vec{k}}]_{2m+2, 2m'+2}$  each, a pair of simultaneous equations for  $[G_{\vec{k}}^{(K)}]_{2m+1, 2m'}$  and  $[G_{\vec{k}}^{(K)}]_{2m+2, 2m'}$ , a pair of simultaneous equations for  $[G_{\vec{k}}^{(K)}]_{2m+1, 2m'+1}$  and  $[G_{\vec{k}}^{(K)}]_{2m+2, 2m'+1}$ , and, finally, a single equation for  $[G_{\vec{k}}^{(K)}]_{2m+2, 2m'+2}$ . These ‘‘block’’ equations should be solved in the order written above since each block equation depends on the solutions to the block equations previous to it.

In summary, our numerical solution can be outlined as follows:

- (1) Set  $m = 0$ .
- (2) Guess the values for  $n_{2m+1}$  and  $n_{2m+2}$ .
- (3) For each  $\vec{k}$ ,

For  $m' = 0, \dots, m$ : Solve block equations.

- (4) Update  $n_{2m+1}$  and  $n_{2m+2}$  from the new  $[G_{\vec{k}}^{(K)}]_{2m+1, 2m'+1}$  and  $[G_{\vec{k}}^{(K)}]_{2m+2, 2m'+2}$  using Eqs. (21) and (22).
- (5) Check for convergence of  $n_{2m+1}$  and  $n_{2m+2}$ : if it is achieved, then set  $m \rightarrow m + 1$  and return to step 2; otherwise, return to step 3 without incrementing  $m$ .

The algorithm outlined above is accurate to fourth order in the time step. This self-consistent approach is advantageous, as one can execute the outer  $\vec{k}$  for-loop in step 3 in parallel, which is the most computationally intensive step of the algorithm. The main computational constraint comes from the time integrals, which require considerable processing and memory resources. If  $d$  is the number of spatial dimensions,  $L$  is the number of sites along a crystal axis, and  $N_t$  is the number of time steps, then the memory requirements scale like  $\binom{d+L/2}{d} N_t^2$ . The binomial coefficient appears as a result of the lattice symmetries and the periodic boundary conditions. Previous nonequilibrium 2PI studies which integrated similar equations of motion did not keep all of the history of the memory kernels for large times, which was justified by the argument that the two-time correlator would damp at an exponential rate [59, 77–80]. We do not make this assumption since it does not always hold for the quench protocols we consider.

### APPENDIX B: PARTICLE NUMBER CONSERVATION

In this Appendix, we identify the terms in the equations of motion that break particle number conservation. We start with Dyson's equation [Eq. (14)], noting that the bare propagator  $G_0$  in this context is the atomic propagator  $\mathcal{G}$ :

$$G_{\vec{k}}^{a_1 a_2, c}(\tau_1, \tau_2) \equiv \mathcal{G}^{a_1 a_2}(\tau_1, \tau_2) + \int_C \int_C d\tau_3 d\tau_4 \mathcal{G}^{a_1 a_3}(\tau_1, \tau_3) \Sigma_{\vec{k}}^{\overline{a_3 a_4}}(\tau_3, \tau_4) G_{\vec{k}}^{a_4 a_2, c}(\tau_4, \tau_2). \quad (\text{B1})$$

Next, we act on both sides with  $\delta(\tau'_1, \tau_1)\{i\partial_{\tau_1} - E_{\vec{k}}\}$ , where, for the moment,  $E_{\vec{k}}$  is an unspecified function of  $\vec{k}$ . We then integrate over  $\tau_1$  and set  $(\tau'_1, \tau_2) = (\tau, \tau^+)$  and  $(a_1, a_2) = (1, 2)$  to get

$$i\frac{\partial}{\partial\tau_1}G_{\vec{k}}^{12,c}(\tau_1 = \tau, \tau_2 = \tau^+) \equiv E_{\vec{k}}G_{\vec{k}}^{12,c}(\tau_1 = \tau, \tau_2 = \tau^+) + \left\{i\frac{\partial}{\partial\tau_1} - E_{\vec{k}}\right\}\mathcal{G}^{12}(\tau_1 = \tau, \tau_2 = \tau^+) + \int_C \int_C d\tau_3 d\tau_4 \left\{i\frac{\partial}{\partial\tau_1} - E_{\vec{k}}\right\}\mathcal{G}^{12}(\tau_1 = \tau, \tau_3)\Sigma_{\vec{k}}^{1\bar{a}}(\tau_3, \tau_4)G_{\vec{k}}^{a2,c}(\tau_4, \tau_2 = \tau^+). \quad (\text{B2})$$

The general form of the contour-time derivative of  $G_{\vec{k}}^{12,c}$  is

$$\begin{aligned} \frac{\partial}{\partial\tau_1}G_{\vec{k}}^{12,c}(\tau_1, \tau_2) &= -i\frac{\partial}{\partial\tau_1}\{\Theta(\tau_1, \tau_2)\langle\hat{a}_{\vec{k}}(\tau_1)\hat{a}_{\vec{k}}^\dagger(\tau_2)\rangle_{\rho_i}^c + \Theta(\tau_2, \tau_1)\langle\hat{a}_{\vec{k}}^\dagger(\tau_2)\hat{a}_{\vec{k}}(\tau_1)\rangle_{\rho_i}^c\} \\ &= -i\delta(\tau_1, \tau_2) - i\Theta(\tau_1, \tau_2)\frac{\partial}{\partial\tau_1}\langle\hat{a}_{\vec{k}}(\tau_1)\hat{a}_{\vec{k}}^\dagger(\tau_2)\rangle_{\rho_i}^c - i\Theta(\tau_2, \tau_1)\frac{\partial}{\partial\tau_1}\langle\hat{a}_{\vec{k}}^\dagger(\tau_2)\hat{a}_{\vec{k}}(\tau_1)\rangle_{\rho_i}^c, \end{aligned} \quad (\text{B3})$$

which also applies to  $\mathcal{G}^{12}$ .

The Dyson's equation can also be rewritten as follows:

$$G_{\vec{k}}^{a_1a_2,c}(\tau_1, \tau_2) \equiv \mathcal{G}^{a_1a_2}(\tau_1, \tau_2) + \int_C \int_C d\tau_3 d\tau_4 G_{\vec{k}}^{a_1a_3,c}(\tau_1, \tau_3)\Sigma_{\vec{k}}^{\bar{a}_3\bar{a}_4}(\tau_3, \tau_4)\mathcal{G}^{a_4a_2}(\tau_4, \tau_2). \quad (\text{B4})$$

We again act on both sides with  $\delta(\tau'_2, \tau_2)\{i\partial_{\tau_2} + E_{\vec{k}}\}$ , integrate over  $\tau_2$ , and set  $(\tau_1, \tau_2) = (\tau, \tau^+)$ ,  $(a_1, a_2) = (1, 2)$  to get

$$i\frac{\partial}{\partial\tau_2}G_{\vec{k}}^{12,c}(\tau_1 = \tau, \tau_2 = \tau^+) \equiv -E_{\vec{k}}G_{\vec{k}}^{12,c}(\tau_1 = \tau, \tau_2 = \tau^+) + \{i\partial_{\tau_2} + E_{\vec{k}}\}\mathcal{G}^{12}(\tau_1 = \tau, \tau_2 = \tau^+) + \int_C \int_C d\tau_3 d\tau_4 G_{\vec{k}}^{1a,c}(\tau_1, \tau_3)\Sigma_{\vec{k}}^{\bar{a}2}(\tau_3, \tau_4)\{i\partial_{\tau_2} + E_{\vec{k}}\}\mathcal{G}^{12,c}(\tau_4, \tau_2 = \tau^+). \quad (\text{B5})$$

Similarly to Eq. (B3), we obtain

$$\frac{\partial}{\partial\tau_2}G_{\vec{k}}^{12,c}(\tau_1, \tau_2) = i\delta(\tau_1, \tau_2) - i\Theta(\tau_1, \tau_2)\frac{\partial}{\partial\tau_2}\langle\hat{a}_{\vec{k}}(\tau_1)\hat{a}_{\vec{k}}^\dagger(\tau_2)\rangle_{\rho_i}^c - i\Theta(\tau_2, \tau_1)\frac{\partial}{\partial\tau_2}\langle\hat{a}_{\vec{k}}^\dagger(\tau_2)\hat{a}_{\vec{k}}(\tau_1)\rangle_{\rho_i}^c. \quad (\text{B6})$$

It then follows from Eqs. (B3) and (B6) that

$$\frac{\partial}{\partial\tau_1}G_{\vec{k}}^{12,c}(\tau_1 = \tau, \tau_2 = \tau^+) + \frac{\partial}{\partial\tau_2}G_{\vec{k}}^{12,c}(\tau_1 = \tau, \tau_2 = \tau^+) = -i\frac{d}{d\tau_1}n_{\vec{k}}(\tau_1 = \tau). \quad (\text{B7})$$

Note that in the special case where  $G_{\vec{k}}^{12,c} = \mathcal{G}^{12}$ , one can show explicitly from the analytical expressions for  $\mathcal{G}^{12}$  (see Appendix C in Ref. [45]) that the right-hand-side of Eq. (B7) vanishes.

Next, by adding Eqs. (B2) and (B5) together, summing over all  $\vec{k}$ , and using Eqs. (B3), (B6), and (B7), we get

$$\begin{aligned} \frac{d}{d\tau_1}\{N(\tau_1 = \tau)\} &= \sum_{\vec{k}} \int_C \int_C d\tau_3 d\tau_4 \left\{i\frac{\partial}{\partial\tau_1} - E_{\vec{k}}\right\}\mathcal{G}^{12}(\tau_1 = \tau, \tau_3)\Sigma_{\vec{k}}^{1\bar{a}}(\tau_3, \tau_4)G_{\vec{k}}^{a2,c}(\tau_4, \tau_2 = \tau^+) \\ &\quad + \sum_{\vec{k}} \int_C \int_C d\tau_3 d\tau_4 G_{\vec{k}}^{1a,c}(\tau_1, \tau_3)\Sigma_{\vec{k}}^{\bar{a}2}(\tau_3, \tau_4)\{i\partial_{\tau_2} + E_{\vec{k}}\}\mathcal{G}^{12,c}(\tau_4, \tau_2 = \tau^+). \end{aligned} \quad (\text{B8})$$

Now, if we set  $E_{\vec{k}} = \epsilon_{\vec{k}} - \mu$  (i.e., we set  $E_{\vec{k}}$  to the single-particle excitation energy of a free particle) and replace  $\mathcal{G}^{12}$  by the free propagator for the BHM obtained when  $U = 0$ , then

$$\left\{i\frac{\partial}{\partial\tau_1} - E_{\vec{k}}\right\}\mathcal{G}^{12}(\tau_1 = \tau, \tau_3) \rightarrow \delta(\tau, \tau_3), \quad (\text{B9})$$

$$\left\{i\frac{\partial}{\partial\tau_2} + E_{\vec{k}}\right\}\mathcal{G}^{12,c}(\tau_4, \tau_2 = \tau^+) \rightarrow -\delta(\tau_4, \tau'), \quad (\text{B10})$$

and Eq. (B8) would become

$$\frac{d}{d\tau_1}N(\tau_1 = \tau) = \sum_{\vec{k}} \int_C d\tau_3 \left\{\Sigma_{\vec{k}}^{1\bar{a}}(\tau, \tau_3)G_{\vec{k}}^{a2,c}(\tau_3, \tau^+) - G_{\vec{k}}^{1a}(\tau, \tau_3)\Sigma_{\vec{k}}^{\bar{a}2}(\tau_3, \tau^+)\right\}. \quad (\text{B11})$$

Baym showed that the term on the right-hand-side of Eq. (B11) vanishes as long as the self-energy  $\Sigma$  is of the form  $\delta\Phi/\delta G$ , with  $\Phi$  a functional of  $G$  [81,82]. As we mention in Sec. III, we obtained our self-energy by taking a functional derivative of the 2PI effective action, which is indeed a functional of  $G$ , hence the right-hand-side of Eq. (B11) vanishes and the particle number



is conserved. It is worth stressing that in this scenario, the self-energy need not be calculated to all orders so that the particle number is conserved. As long as the approximation of the self-energy is of the form  $\delta\Phi/\delta G$ , even after taking some low-energy approximation as we do in our ET, conservation will still be guaranteed.

In our case,  $\mathcal{G}^{12}$  is not the free propagator for the BHM obtained when  $U = 0$  but, instead, is the atomic propagator obtained in the limit when  $J = 0$ . Hence there exists no function  $E_{\vec{k}}$  in which Eqs. (B9) and (B10) could possibly be satisfied. The reason for this is due to the asymmetry between the single-particle and the hole excitation energies. For the free propagator,  $E^{(+)} = -E^{(-)}$ , where  $E^{(+)}$  and  $E^{(-)}$  are the single-particle and hole excitation energies, respectively, whereas for the atomic propagator  $\mathcal{G}^{12}$ ,  $E^{(+)} \neq -E^{(-)}$  for all values of  $\mu$ . Due to this asymmetry, additional terms are generated, leading to

$$\begin{aligned} \frac{d}{d\tau_1} N(\tau_1 = \tau) &= i \sum_{\vec{k}} \int_C \int_C d\tau_3 d\tau_4 [\partial_{\tau_1} \mathcal{G}^{12}] (\tau_1 = \tau, \tau_3) \Sigma_{\vec{k}}^{1\bar{a}} (\tau_3, \tau_4) G_{\vec{k}}^{a2,c} (\tau_4, \tau_2 = \tau^+) \\ &+ i \sum_{\vec{k}} \int_C \int_C d\tau_3 d\tau_4 G_{\vec{k}}^{1a,c} (\tau_1, \tau_3) \Sigma_{\vec{k}}^{\bar{a}2} (\tau_3, \tau_4) [\partial_{\tau_2} \mathcal{G}^{12}] (\tau_4, \tau_2 = \tau^+), \end{aligned} \quad (\text{B12})$$

where we introduce the shorthand notation

$$[\partial_{\tau_1}] G_{\vec{k}}^{12,c} (\tau_1, \tau_2) = -i \Theta(\tau_1, \tau_2) \frac{\partial}{\partial \tau_1} \langle \hat{a}_{\vec{k}}^{\dagger}(\tau_1) \hat{a}_{\vec{k}}^{\dagger}(\tau_2) \rangle_{\hat{\rho}_i}^c - i \Theta(\tau_2, \tau_1) \frac{\partial}{\partial \tau_1} \langle \hat{a}_{\vec{k}}^{\dagger}(\tau_2) \hat{a}_{\vec{k}}^{\dagger}(\tau_1) \rangle_{\hat{\rho}_i}^c, \quad (\text{B13})$$

$$[\partial_{\tau_2}] G_{\vec{k}}^{12,c} (\tau_1, \tau_2) = -i \Theta(\tau_1, \tau_2) \frac{\partial}{\partial \tau_2} \langle \hat{a}_{\vec{k}}^{\dagger}(\tau_1) \hat{a}_{\vec{k}}^{\dagger}(\tau_2) \rangle_{\hat{\rho}_i}^c - i \Theta(\tau_2, \tau_1) \frac{\partial}{\partial \tau_2} \langle \hat{a}_{\vec{k}}^{\dagger}(\tau_2) \hat{a}_{\vec{k}}^{\dagger}(\tau_1) \rangle_{\hat{\rho}_i}^c, \quad (\text{B14})$$

where we now set  $E_{\vec{k}} \rightarrow 0$ , as it serves no purpose for us anymore. The terms on the right-hand side of (B12) are in general not 0. If we kept all terms in the ET and did not make the low-energy approximation, then the right-hand-side of (B12) should equal 0. However, because the bare propagator we use is the atomic propagator, Baym's arguments do not hold in the low-energy theory and there is not conservation of the particle number.

- 
- [1] I. Bloch, *Nat. Phys.* **1**, 23 (2005).  
 [2] D. Jaksch and P. Zoller, *Ann. Phys.* **315**, 52 (2005).  
 [3] O. Morsch and M. Oberthaler, *Rev. Mod. Phys.* **78**, 179 (2006).  
 [4] M. Lewenstein, A. Sanpera, V. Ahufinger, B. Damski, A. Sen, and U. Sen, *Adv. Phys.* **56**, 243 (2007).  
 [5] I. Bloch, J. Dalibard, and W. Zwerger, *Rev. Mod. Phys.* **80**, 885 (2008).  
 [6] M. P. Kennett, *ISRN Condens. Matter Phys.* **2013**, 393616 (2013).  
 [7] D. Jaksch, C. Bruder, J. I. Cirac, C. W. Gardiner, and P. Zoller, *Phys. Rev. Lett.* **81**, 3108 (1998).  
 [8] M. P. A. Fisher, P. B. Weichman, G. Grinstein, and D. S. Fisher, *Phys. Rev. B* **40**, 546 (1989).  
 [9] M. Greiner, O. Mandel, T. Esslinger, T. W. Hänsch, and I. Bloch, *Nature* **415**, 39 (2002).  
 [10] D. Chen, M. White, C. Borries, and B. DeMarco, *Phys. Rev. Lett.* **106**, 235304 (2011).  
 [11] C.-L. Hung, X. Zhang, N. Gemelke, and C. Chin, *Phys. Rev. Lett.* **104**, 160403 (2010).  
 [12] W. S. Bakr, A. Peng, M. E. Tai, R. Ma, J. Simon, J. I. Gillen, S. Fölling, L. Pollet, and M. Greiner, *Science* **329**, 547 (2010).  
 [13] T. W. B. Kibble, *J. Phys. A* **9**, 1387 (1976).  
 [14] W. H. Zurek, *Nature* **317**, 505 (1985).  
 [15] W. H. Zurek, U. Dorner, and P. Zoller, *Phys. Rev. Lett.* **95**, 105701 (2005).  
 [16] S. R. Clark and D. Jaksch, *Phys. Rev. A* **70**, 043612 (2004).  
 [17] C. Kollath, A. M. Läuchli, and E. Altman, *Phys. Rev. Lett.* **98**, 180601 (2007).  
 [18] B. Sciolla and G. Biroli, *Phys. Rev. Lett.* **105**, 220401 (2010).  
 [19] B. Sciolla and G. Biroli, *J. Stat. Mech.* (2011) P11003.  
 [20] U. R. Fischer, R. Schützhold, and M. Uhlmann, *Phys. Rev. A* **77**, 043615 (2008).  
 [21] U. R. Fischer and R. Schützhold, *Phys. Rev. A* **78**, 061603 (2008).  
 [22] M. P. Kennett and D. Dalidovich, *Phys. Rev. A* **84**, 033620 (2011).  
 [23] H. U. R. Strand, M. Eckstein, and P. Werner, *Phys. Rev. X* **5**, 011038 (2015).  
 [24] I. S. Landea and N. Nesi, *Phys. Rev. A* **91**, 063601 (2015).  
 [25] A. Polkovnikov, *Phys. Rev. B* **72**, 161201 (2005).  
 [26] S. S. Natu, K. R. A. Hazzard, and E. J. Mueller, *Phys. Rev. Lett.* **106**, 125301 (2011).  
 [27] J.-S. Bernier, G. Roux, and C. Kollath, *Phys. Rev. Lett.* **106**, 200601 (2011).  
 [28] S. S. Natu and E. J. Mueller, *Phys. Rev. A* **87**, 063616 (2013).  
 [29] J.-S. Bernier, D. Poletti, P. Barmettler, G. Roux, and C. Kollath, *Phys. Rev. A* **85**, 033641 (2012).  
 [30] J. Zakrzewski, *Phys. Rev. A* **71**, 043601 (2005).  
 [31] C. Trefzger and K. Sengupta, *Phys. Rev. Lett.* **106**, 095702 (2011).  
 [32] Y. Yanay and E. J. Mueller, *Phys. Rev. A* **93**, 013622 (2016).  
 [33] E. H. Lieb and D. W. Robinson, *Commun. Math. Phys.* **28**, 251 (1972).  
 [34] G. Carleo, F. Becca, L. Sanchez-Palencia, S. Sorella, and M. Fabrizio, *Phys. Rev. A* **89**, 031602 (2014).  
 [35] A. M. Läuchli and C. Kollath, *J. Stat. Mech.* (2008) P05018.  
 [36] P. Barmettler, D. Poletti, M. Cheneau, and C. Kollath, *Phys. Rev. A* **85**, 053625 (2012).  
 [37] K. V. Krutitsky, P. Navez, F. Queisser, and R. Schützhold, *Eur. Phys. J. Quant. Tech.* **1**, 12 (2014).  
 [38] M. Cheneau, P. Barmettler, D. Poletti, M. Endres, P. Schauß, T. Fukuhara, C. Gross, I. Bloch, C. Kollath, and S. Kuhr, *Nature* **481**, 484 (2012).  
 [39] P. Navez and R. Schützhold, *Phys. Rev. A* **82**, 063603 (2010).

- [40] S. Trotzky, Y.-A. Chen, A. Flesch, I. P. McCulloch, U. Schollwöck, J. Eisert, and I. Bloch, *Nat. Phys.* **8**, 325 (2012).
- [41] L. Amico and V. Penna, *Phys. Rev. B* **62**, 1224 (2000).
- [42] A. Dutta, C. Trefzger, and K. Sengupta, *Phys. Rev. B* **86**, 085140 (2012).
- [43] C. Schroll, F. Marquardt, and C. Bruder, *Phys. Rev. A* **70**, 053609 (2004).
- [44] F. Queisser, K. V. Krutitsky, P. Navez, and R. Schützhold, *Phys. Rev. A* **89**, 033616 (2014).
- [45] M. R. C. Fitzpatrick and M. P. Kennett, *Nucl. Phys. B* **930**, 1 (2018).
- [46] K. Sengupta and N. Dupuis, *Phys. Rev. A* **71**, 033629 (2005).
- [47] O. V. Konstantinov and V. I. Perel, *Zh. Eksp. Teor. Fiz.* **39**, 197 (1960) [*Sov. Phys. JETP* **12**, 142 (1961)].
- [48] J. Schwinger, *J. Math. Phys.* **2**, 407 (1961).
- [49] L. V. Keldysh, *Zh. Eksp. Teor. Fiz.* **47**, 1515 (1964) [*Sov. Phys. JETP* **20**, 1018 (1965)].
- [50] J. Rammer and H. Smith, *Rev. Mod. Phys.* **58**, 323 (1986).
- [51] A. J. Niemi and G. W. Semenoff, *Ann. Phys.* **152**, 105 (1984).
- [52] N. P. Landsman and C. G. van Weert, *Phys. Rep.* **145**, 141 (1987).
- [53] K.-c. Chou, Z.-b. Su, B.-l. Hao, and L. Yu, *Phys. Rep.* **118**, 1 (1985).
- [54] A. Robertson, V. M. Galitski, and G. Refael, *Phys. Rev. Lett.* **106**, 165701 (2011).
- [55] D. Dalidovich and M. P. Kennett, *Phys. Rev. A* **79**, 053611 (2009).
- [56] T. D. Graß, F. E. A. dos Santos, and A. Pelster, *Laser Phys.* **21**, 1459 (2011).
- [57] T. D. Graß, F. E. A. dos Santos, and A. Pelster, *Phys. Rev. A* **84**, 013613 (2011).
- [58] T. D. Graß, Master's thesis, Freie Universität, Berlin (2009).
- [59] A. M. Rey, B. L. Hu, E. Calzetta, A. Roura, and C. W. Clark, *Phys. Rev. A* **69**, 033610 (2004).
- [60] A. M. Rey, B. L. Hu, E. Calzetta, and C. W. Clark, *Phys. Rev. A* **72**, 023604 (2005).
- [61] K. Temme and T. Gasenzer, *Phys. Rev. A* **74**, 053603 (2006).
- [62] E. Calzetta, B. L. Hu, and A. M. Rey, *Phys. Rev. A* **73**, 023610 (2006).
- [63] A. Polkovnikov, *Phys. Rev. A* **68**, 053604 (2003).
- [64] N. Lo Gullo and L. Dell'Anna, *Phys. Rev. B* **94**, 184308 (2016).
- [65] N. Dupuis, *Nucl. Phys. B* **618**, 617 (2001).
- [66] A. S. Sajnna and R. Micnas, *Phys. Rev. A* **97**, 033605 (2018).
- [67] J. M. Cornwall, R. Jackiw, and E. Tomboulis, *Phys. Rev. D* **10**, 2428 (1974).
- [68] W. Zwerger, *J. Opt. B* **5**, S9 (2003).
- [69] D. Sen, K. Sengupta, and S. Mondal, *Phys. Rev. Lett.* **101**, 016806 (2008).
- [70] R. Katani and S. Shahmorad, *Appl. Math. Model.* **34**, 400 (2010).
- [71] C. Guo, I. de Vega, U. Schollwöck, and D. Poletti, *Phys. Rev. A* **97**, 053610 (2018).
- [72] M. White, M. Pasienski, D. McKay, S. Q. Zhou, D. Ceperley, and B. DeMarco, *Phys. Rev. Lett.* **102**, 055301 (2009).
- [73] M. Pasienski, D. McKay, M. White, and B. DeMarco, *Nat. Phys.* **6**, 677 (2010).
- [74] J.-Y. Choi, S. Hild, J. Zeiher, P. Schauß, A. Rubio-Abadal, T. Yefsah, V. Khemani, D. A. Huse, I. Bloch, and C. Gross, *Science* **352**, 1547 (2016).
- [75] C. Meldgin, U. Ray, P. Russ, D. Chen, D. M. Ceperley, and B. DeMarco, *Nat. Phys.* **12**, 646 (2016).
- [76] A. Rubio-Abadal, J.-Y. Choi, J. Zeiher, S. Hollerith, J. Rui, I. Bloch, and C. Gross, [arXiv:1805.00056v1](https://arxiv.org/abs/1805.00056v1).
- [77] J. Berges and J. Cox, *Phys. Lett. B* **517**, 369 (2001).
- [78] G. Aarts and J. Berges, *Phys. Rev. D* **64**, 105010 (2001).
- [79] G. Aarts, D. Ahrensmeier, R. Baier, J. Berges, and J. Serreau, *Phys. Rev. D* **66**, 045008 (2002).
- [80] J. Berges, *Nucl. Phys. A* **699**, 847 (2002).
- [81] G. Baym, *Phys. Rev.* **127**, 1391 (1962).
- [82] G. Stefanucci and R. van Leeuwen, *Nonequilibrium Many-Body Theory of Quantum Systems* (Cambridge University Press, New York, 2013).

*Correction:* The previously published Figs. 2 and 3 contained errors in the curve keys and have been replaced.